







Exciton-polaron Rydberg states in monolayer MoSe₂ and WSe₂

Erfu Liu ^{1,7}, Jeremiah van Baren^{1,7}, Zhengguang Lu^{2,3}, Takashi Taniguchi ⁴, Kenji Watanabe ⁵, Dmitry Smirnov ², Yia-Chung Chang ⁶✉ & Chun Hung Lui ¹✉

Exciton polaron is a hypothetical many-body quasiparticle that involves an exciton dressed with a polarized electron-hole cloud in the Fermi sea. It has been evoked to explain the excitonic spectra of charged monolayer transition metal dichalcogenides, but the studies were limited to the ground state. Here we measure the reflection and photoluminescence of monolayer MoSe₂ and WSe₂ gating devices encapsulated by boron nitride. We observe gate-tunable exciton polarons associated with the 1s–3s exciton Rydberg states. The ground and excited exciton polarons exhibit comparable energy redshift (15–30 meV) from their respective bare excitons. The robust excited states contradict the trion picture because the trions are expected to dissociate in the excited states. When the Fermi sea expands, we observe increasingly severe suppression and steep energy shift from low to high exciton-polaron Rydberg states. Their gate-dependent energy shifts go beyond the trion description but match our exciton-polaron theory. Our experiment and theory demonstrate the exciton-polaron nature of both the ground and excited excitonic states in charged monolayer MoSe₂ and WSe₂.

¹Department of Physics and Astronomy, University of California, Riverside, CA 92521, USA. ²National High Magnetic Field Laboratory, Tallahassee, FL 32310, USA. ³Department of Physics, Florida State University, Tallahassee, FL 32310, USA. ⁴International Center for Materials Nanoarchitectonics, National Institute for Materials Science, 1-1 Namiki Tsukuba, Ibaraki 305-0044, Japan. ⁵National Institute for Materials Science, 1-1 Namiki Tsukuba, Ibaraki 305-0044, Japan. ⁶Research Center for Applied Sciences, Academia Sinica, Taipei 11529, Taiwan. ⁷These authors contributed equally: Erfu Liu, Jeremiah van Baren. ✉email: yiachang@gate.sinica.edu.tw; joshua.lui@ucr.edu

Hydrogen atoms are known to exhibit the Rydberg spectrum, which played a crucial role in the birth and development of quantum mechanics. As the solid-state counterpart of hydrogen atoms, excitons can also exhibit Rydberg-like optical spectra, which are crucial to revealing the exciton quantum structure. In principle, Rydberg-like spectra can also exist in complex excitonic states strongly coupled to the Fermi sea (FS), despite the lack of experimental evidence. Such spectra are expected to exhibit distinctive characteristics originating from the complex many-body interactions, which can help us understand the nature of coupled states between excitons and FS.

In a conventional scenario of exciton–FS interactions, the exciton captures an extra charge to form a three-body bound state called a trion (Fig. 1), in analogy to the hydrogen ion^{1–3}. The trion picture has been widely applied to explain the optical spectra of charged semiconductors, such as quantum wells^{4–6}, carbon nanotubes⁷, and two-dimensional (2D) transition metal dichalcogenides^{8–11}. Recent research, however, points out that the three-particle picture may be inadequate to account for the complex exciton–FS interactions^{12–20}. In a more realistic description, an exciton can excite many electron–hole pairs in the FS (Fig. 1). When the exciton is coupled to the FS electron–hole pairs, it can form a complex quasiparticle called exciton polaron^{14–18} (not the conventional polarons dressed by phonons). The exciton polaron is fundamentally different from the trion. First, the exciton polarons are charge-neutral bosons, whereas the trions are fermions with net electric charge. Second, a general exciton-polaron state is a linear combination of a bare exciton, an exciton dressed with one FS electron–hole pair (called a Suris tetron), and higher-order components that represent an exciton dressed with two and more FS electron–hole pairs (Fig. 1). Such a many-body configuration contrasts with the simple three-particle configuration of the trion.

There have been ongoing debates to distinguish the trion and exciton-polaron pictures, because they give similar energy in the low-charge-density or weak-coupling regime. For instance, a Suris tetron can be viewed as a trion bound with a FS hole (Fig. 1)^{12–14}. When the FS is small, the trion–hole binding is weak, and hence the polaron has almost the same binding energy as the trion. However, the trion and polaron binding energies become

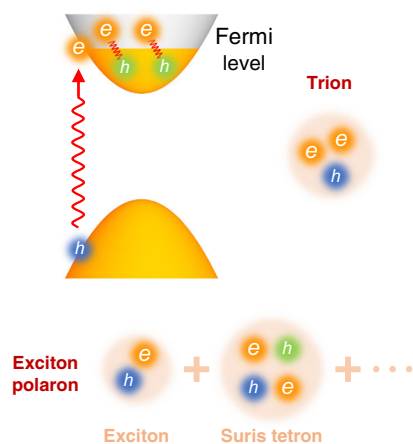


Fig. 1 Schematic of trion and exciton polaron. When a photo-generated exciton interacts with the Fermi sea (FS), it can excite many electron–hole pairs on the FS. The trion is a bound state between an exciton and one FS electron. The exciton-polaron state is the linear combination of a bare exciton, an exciton dressed with one FS electron–hole pair (Suris tetron), and higher-order components that represent an exciton dressed with two and more FS electron–hole pairs.

markedly different under strong exciton–FS coupling, which can be realized in two ways: (1) enlarging the FS (e.g., by electrostatic gating) and (2) increasing the exciton size (e.g., by using excited Rydberg exciton states). It would therefore be interesting to investigate excited excitonic Rydberg states coupled to a tunable FS, but the related experimental studies have been lacking.

In this article, we apply both approaches to investigate the ground and excited excitonic Rydberg states coupled to the gate-tunable FS in monolayer MoSe₂ and WSe₂ devices. By using reflectance contrast and photoluminescence (PL) spectroscopy, we observe optical signatures of the exciton-polaron states associated with the 1s–3s Rydberg excitons and characterize their gate-dependent optical properties. We also establish a comprehensive exciton-polaron theory to quantitatively explain our results. Our experiment and theory support the exciton-polaron picture rather than the commonly used trion picture. The observation of exciton-polaron Rydberg states shall significantly enrich the excitonic physics in 2D semiconductors.

Results and discussion

Exciton Rydberg states in monolayer MoSe₂. We investigate ultraclean monolayer MoSe₂ single-gate devices encapsulated by hexagonal boron nitride (BN) and equipped with thin graphite as the contact and back-gate electrodes (see “Methods” and Supplementary Fig. 1). Monolayer MoSe₂ possesses a direct bandgap in two valleys, where the conduction (valence) band is split into two subbands with ~30 meV (~180 meV) separation by spin–orbit coupling²¹. The inner and outer subbands produce the *A* and *B* bright excitons, respectively (Fig. 2a). Each exciton hosts a series of internal energy levels, analogous to the hydrogenic Rydberg levels (Fig. 2b)^{22–28}. We have measured the PL at magnetic fields $B = -31$ T to $+31$ T and the gate voltage $V_g = 0$ V (Fig. 2c). We observe the *A*-exciton and *B*-exciton 1s states (A_{1s} , B_{1s}) and, between them, the *A*-exciton 2s and 3s states (A_{2s} , A_{3s})^{26–28}. From the magnetic-field-dependent exciton energies, we extract the linear Zeeman shift and quadratic diamagnetic shift^{27–30}. A_{2s} and A_{3s} excitons exhibit noticeable diamagnetic shift, from which we can derive their root-mean-square radii $r_{2s} = 3.2$ nm and $r_{3s} = 8.1$ nm (Fig. 2d). The A_{1s} diamagnetic shift is too small to be discerned in our experiment. But from the extracted r_{2s} and r_{3s} value, we can apply a model calculation to deduce the A_{1s} root-mean-square radius to be $r_{1s} = 1.1$ nm, which matches the experimental value in the literature²⁷ (Supplementary Table 1).

PL and reflectance contrast measurements on monolayer MoSe₂.

We have measured the gate-dependent reflectance contrast ($\Delta R/R$) and PL maps of monolayer MoSe₂, which reveal the absorption and emission properties of the material, respectively (Fig. 3 and Supplementary Figs. 2–4; see “Methods”). We further take the second energy derivative of the reflectance contrast $d^2(\Delta R/R)/dE^2$ to sharpen the weak features (Fig. 3e–h). We observe that the A_{1s-3s} and B_{1s} excitons subside on the electron (–) and hole (+) sides and below them emerge new pairs of features labeled as A_{1-3}^\pm and B_1^\pm , respectively (Fig. 3; A_3^\pm are observed only in PL). Our gate-dependent results contrast with and complement the early report of a trion excited state at an unknown doping level in monolayer WS₂³¹.

A_{1-3}^\pm and B_1^\pm exhibit intriguing gate-dependent optical intensity. We first compare the A_{1-3}^\pm and B_1^\pm absorption properties inferred from the second-order differential reflectance contrast maps (Fig. 3e–h). A_{1-3}^\pm are suppressed at $|V| > 4$ V. Such gate-induced suppression is widely known, but the underlying mechanism is still uncertain. Here we can gain some insight by comparing A_{1-3}^\pm and B_1^\pm . B_1^\pm are less suppressed than A_{1-3}^\pm , and B_1^\pm

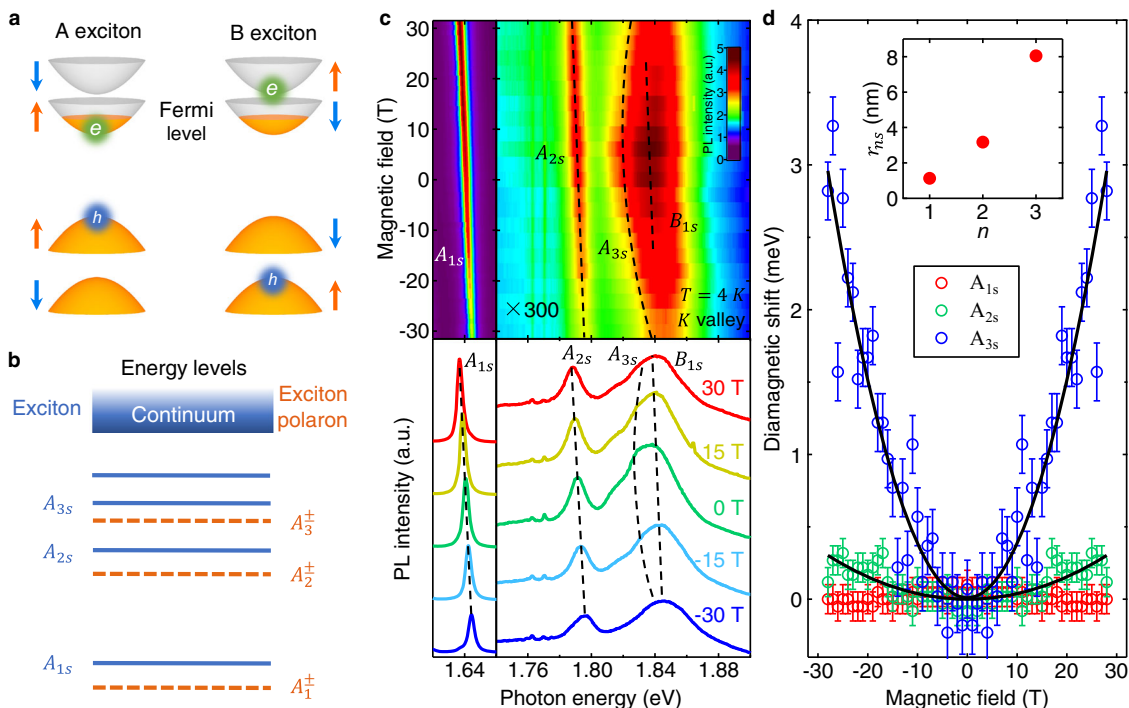


Fig. 2 Excitonic states in monolayer MoSe₂. **a** The band configurations of A and B bright excitons in monolayer MoSe₂. The arrows denote the electron spin of the bands. The Fermi level reaches only the inner subbands in our experiment. **b** The internal energy levels of exciton and exciton polaron. **c** Magnetic-field-dependent PL maps of monolayer MoSe₂ plotted in arbitrary unit (a.u.) at zero gate voltage and temperature $T = 4$ K. The lower panel shows the cross-cut PL spectra at five different magnetic fields. The dashed lines highlight the exciton energy shifts. The PL intensity in 1.74–1.90 eV is magnified 300 times for clarity. **d** The diamagnetic energy shift of the A-exciton 1s, 2s, and 3s states (denoted by red, green, and blue circles, respectively) as a function of the magnetic field. The error bars represent the uncertainty in fitting the PL spectra with multiple Lorentzian functions. The lines are quadratic fits. The inset shows the root-mean-square exciton radii (r_{ns}) for the principal quantum number $n = 1, 2, 3$. r_{2s} and r_{3s} are extracted from the diamagnetic shifts. r_{1s} is obtained by a theoretical model and it matches the experimental value in ref. ²⁷.

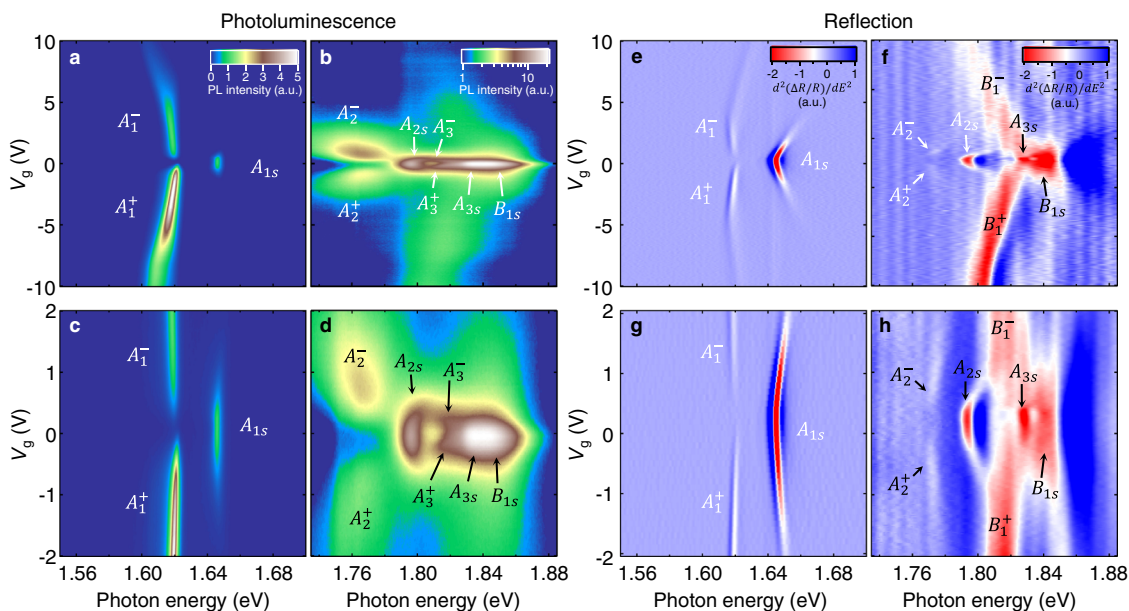


Fig. 3 Optical signatures of exciton-polaron Rydberg states in monolayer MoSe₂. **a, b** Gate-dependent PL maps. **c, d** Zoom-in PL maps for gate voltages $V_g = -2$ to $+2$ V. **a, c** share the same color scale bar; **b, d** share the same log-scale color bar. **e, f** Gate-dependent maps of the second energy derivative of the reflectance contrast $d^2(\Delta R/R)/dE^2$. **g, h** Zoom-in $d^2(\Delta R/R)/dE^2$ maps for $V_g = -2$ to $+2$ V. **e-h** share the same color scale bar. The intensity of the spectra in **b, d (f, h)** is magnified 300 (20) times. The measurements were made at sample temperature $T \approx 15$ K with no magnetic field. All PL intensity and $d^2(\Delta R/R)/dE^2$ values are plotted in arbitrary units (a.u.).

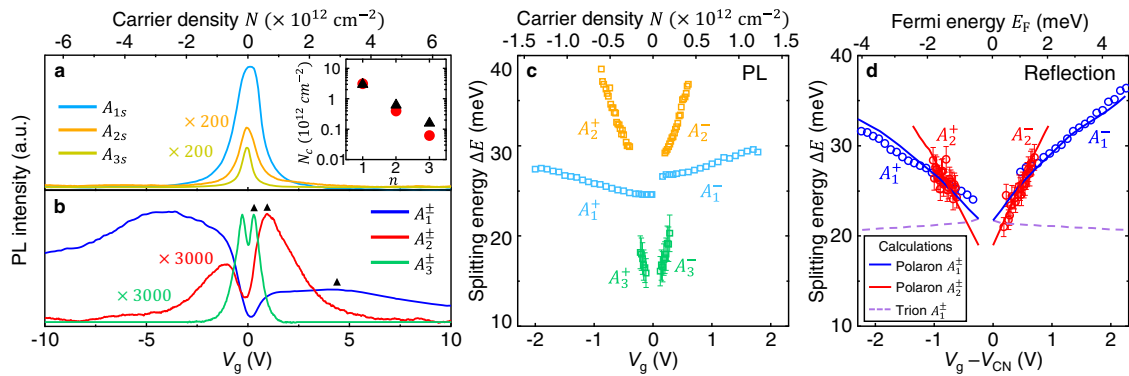


Fig. 4 Gate-dependent optical characteristics of ground and excited exciton polarons in monolayer MoSe₂. **a, b** Gate-dependent integrated PL intensity of excitons and exciton polarons, plotted in arbitrary unit (a.u.), as a function of gate voltage (bottom axis) and charge density (top axis). The charge neutrality point is at $V_g = 0$ V. We magnify the A_{2s} , A_{3s} (A_2^\pm , A_3^\pm) PL intensity 200 (3000) times for clarity. The inset shows the charge density at maximum PL intensity in **b** (black triangles), compared to the quenching charge density (red dots) expected from the state-filling effect with the exciton radii in Fig. 1d. **c** Gate-dependent PL splitting energy between A_1^\pm , A_2^\pm , A_3^\pm and A_{1s} , A_{2s} , A_{3s} , respectively (denoted by cyan, orange, and green squares, respectively). **d** Gate-dependent splitting energies between the A_1^\pm and A_{1s} absorption peaks (blue circles) and between the A_2^\pm and A_{2s} reflection features (red circles). The charge neutrality point is at $V_{CN} \approx 0.25$ V, which has been subtracted from V_g . The purple dashed lines are the calculated trion binding energy. The blue (red) solid lines are the calculated A_1^\pm (A_2^\pm) binding energies by our theoretical model of exciton polaron. The error bars (not shown if smaller than the symbols) in **c** (**d**) represent the uncertainty in fitting the PL (reflection) features.

Table 1 Measured binding energies of exciton polarons for monolayer MoSe₂.

		A_1^-	A_1^+	A_2^-	A_2^+	A_3^-	A_3^+
PL	ΔE ($E_F = 0$)	26.1 ± 0.1	24.3 ± 0.1	24.6 ± 0.2	22.7 ± 0.4	13.0 ± 0.5	13.1 ± 0.3
	$d(\Delta E)/dE_F$	1.10 ± 0.07	-0.75 ± 0.05	11.1 ± 0.6	-7.9 ± 0.6	13.7 ± 2.3	-23.8 ± 1.6
Reflection	ΔE ($E_F = 0$)	23.1 ± 0.2	23.7 ± 0.1	16.4 ± 0.7	22.6 ± 1.0	—	—
	$d(\Delta E)/dE_F$	2.9 ± 0.1	-1.91 ± 0.06	7.0 ± 1.0	-2.9 ± 1.6	—	—

ΔE ($E_F = 0$) denotes the energy separation (in the unit of meV) between the exciton and exciton polaron at the charge neutrality point. $d(\Delta E)/dE_F$ denotes the slope of ΔE with respect to the Fermi energy (E_F).

remains prominent on the hole side (Fig. 3f). Exciton suppression usually comes from two effects: (1) the plasma screening effect—free charges screen the Coulomb interaction; (2) the state-filling effect—carriers occupy the band-edge states that are needed to form excitons. *A* and *B* excitonic states experience similar screening effects because they share the same dielectric environment. But they have different state-filling effects, because the injected carriers can block the *A* excitons in the inner subbands but not the *B* excitons in the outer subbands (Fig. 2a and Supplementary Fig. 5). Such a difference is more prominent on the hole side than on the electron side due to the large valence-band splitting. Correspondingly, we observe stronger gate-induced suppression on A_1^\pm than on B_1^\pm , on the hole side than on the electron side. The state-filling effect should therefore be the major suppression mechanism. Gate-induced suppression is also found in PL, but the *A*–*B* contrast is less pronounced (Fig. 3).

Gate-dependent properties of the exciton-polaron Rydberg states in monolayer MoSe₂. We next compare A_1^\pm , A_2^\pm , and A_3^\pm . Figure 4a, b displays the gate-dependent excitonic PL intensity. When the charge density increases, A_{1s} , A_{2s} , and A_{3s} quickly subside, but A_1^\pm , A_2^\pm , and A_3^\pm first grow and then diminish. Their respective critical charge density (N_c), defined at maximum PL, decreases monotonically from $N_1 \approx 3 \times 10^{12}$ cm⁻², $N_2 \approx 6.2 \times 10^{11}$ cm⁻² to $N_3 \approx 1.6 \times 10^{11}$ cm⁻² on the electron side (black triangles in Fig. 4a, b); the suppression increases from low to high Rydberg states. The observation can be roughly explained by the increasing state-filling effect from low to high states. High Rydberg excitons have larger spatial size and smaller *k*-space

extent than low Rydberg excitons. From our extracted radii of A_{1s} , A_{2s} , and A_{3s} excitons (inset of Fig. 2d)²⁷, we estimate their radii in the *k*-space to be $k_{1s} \approx 0.44$ nm⁻¹, $k_{2s} \approx 0.16$ nm⁻¹ and $k_{3s} \approx 0.062$ nm⁻¹ by the uncertainty relation $\Delta x \Delta k \approx 1/2$. The corresponding charge density to block the *k*-space of these excitons decreases from $N_{1s} \approx 3.1 \times 10^{12}$ cm⁻², $N_{2s} \approx 3.9 \times 10^{11}$ cm⁻² to $N_{3s} \approx 6.1 \times 10^{10}$ cm⁻² (red dots in the inset of Fig. 4a), when we consider the relation $N = k^2/2\pi$ for 2D quadratic bands with valley degeneracy. These value roughly match our measured critical charge density (inset of Fig. 4a) and hence support that A_1^\pm , A_2^\pm , A_3^\pm are associated with the A_{1s} , A_{2s} , A_{3s} excitons, respectively.

In addition to the gate-dependent suppression, the Rydberg states also exhibit remarkable gate-dependent energy shifts. Figure 3c, d displays the splitting energies (ΔE) between A_1^\pm , A_2^\pm , A_3^\pm and A_{1s} , A_{2s} , A_{3s} , respectively, as a function of gate voltage V_g , charge density N , and Fermi energy E_F . Their different splitting energies at $E_F = 0$ (i.e., the exciton-polaron binding energy) and their slope with respect to E_F are summarized in Table 1. The slope of ΔE increases from low to high Rydberg states, indicating increasing exciton–FS interaction from low to high states.

Calculations of exciton polarons for monolayer MoSe₂. To clarify the nature of A_{1-3}^\pm states, we have calculated the absorption resonances of A_{1s} , A_{2s} , A_1^\pm , and A_2^\pm states by first-principles calculations based on both the trion picture and exciton-polaron picture (see the details in Supplementary Note 7). Our calculations apply a realistic long-range Coulomb potential and consider

the carrier screening effect, state-filling effect, and the band-structure renormalization by the FS²⁹. The calculated A_1^\pm trion binding energy decreases with the gate voltage V_g due to the increasing charge screening and state-filling effect at increasing carrier density (dashed lines in Fig. 4d). The result contradicts our observation that both the excitonic splitting energies ΔE_1 and ΔE_2 increase with carrier density. The trion picture is therefore unable to explain the E_F dependence of ΔE_1 and ΔE_2 .

Our calculations based on the exciton-polaron theory produce markedly different results (solid lines in Fig. 4d and Supplementary Figs. 7 and 8). In our theory, we only consider an exciton polaron as the linear combination of a bare exciton and a Suris tetron (Fig. 1 and Supplementary Note 7); a Suris tetron is a four-particle bound state that represents an exciton coupled to one FS electron-hole pair^{12, 13} (Fig. 1). The higher-order components, which represent an exciton coupled to two and more FS electron-hole pairs, are neglected in our model. Such a simplification is justified, because, after an exciton becomes a Suris tetron, its coupling to additional FS electron-hole pairs is much reduced due to screening. The higher-order terms are important only in very high carrier density.

In our theory, there are two branches of exciton polarons with different compositions of the bare exciton and the Suris tetron^{12–15}. At the low-charge-density regime, the higher-energy branch is dominated by the bare exciton component and hence exhibits strong oscillator strength; the lower-energy branch is dominated by the Suris tetron component and exhibits weak oscillator strength. As the charge density increases, the exciton component in the lower branch will increase, and the Suris tetron component in the higher branch will increase, leading to a transfer of oscillator strength from the higher to lower branch (Supplementary Figs. 7 and 8).

The energy separation between the two exciton-polaron branches is here defined as the binding energy of the exciton polaron. To compare the binding energies of trion and exciton polaron, we may consider a Suris tetron as a trion bound with a FS hole (in the case of electron FS). In the low-charge-density limit, the trion-hole binding is negligible due to the small phase space of the FS. As a result, the exciton-polaron binding energy (e.g., the energy difference between a bare exciton and a Suris tetron) is reduced to the trion binding energy (Fig. 4d). But when the FS expands, the enlarged phase space of the FS hole increases the trion-hole binding, which contributes to the total polaron binding. In addition, the coupling between the bare exciton and Suris tetron increases as the FS expands, further widening the separation between the two polaron branches^{14, 15}. Consequently, the exciton-polaron binding energy increases with the charge density, unlike the trion binding energy that decreases with the charge density.

We have calculated the splitting energy between the two polaron branches (i.e., the polaron binding energy) for both the ground and excited states in monolayer MoSe₂ (solid lines in Fig. 4d). We note that, for a monolayer semiconductor embedded in BN, a large fraction of the electric field between carriers goes out of the semiconductor plane; this reduces the in-plane free-carrier screening and the reduction of screening increases with the exciton size²². Our calculation uses different values of an adjustable parameter f to account for the different reduction of screening in the ground and excited states. By using the best-fit value $f=0.05$ (0.025) for the ground (excited) states, our calculations can quantitatively reproduce the increasing splitting energy with charge density for both the ground and excited states (Fig. 4d and see the details in Supplementary Note 7). The experiment-theory agreement strongly supports the exciton-polaron nature of the states.

Exciton-polaron Rydberg states in monolayer WSe₂. We have also observed exciton-polaron Rydberg states in monolayer WSe₂. Figure 5a–d displays the gate-dependent PL maps and second-order differential reflectance contrast maps of a BN-encapsulated monolayer WSe₂ device. The results reveal the 1s–4s exciton Rydberg states in the charge neutrality region^{27–30, 32, 33}. As we tune the Fermi level away from charge neutrality, we observe the exciton polarons (A_1^\pm , A_2^\pm) associated with the 1s and 2s exciton states, as well as a somewhat obscured PL signature of the polaron (A_3^\pm) associated with the 3s exciton state.

Compared to monolayer MoSe₂, the exciton polarons in monolayer WSe₂ exhibit one distinct feature. That is, in monolayer WSe₂, while the exciton polarons appear on both the electron and hole sides of the reflection data, the excited-state polarons appear only on the hole side of the PL data (Fig. 5a–d). The mechanism of such an electron-hole asymmetry of excited polarons is unknown at this stage. We speculate that it is related to the opposite spin configuration of the conduction bands in monolayer WSe₂ compared to that in monolayer MoSe₂ (Fig. 2a and inset of Fig. 5a). Prior studies^{34–42} have shown that the opposite spin of conduction bands in monolayer WSe₂ give rise to dark excitons (D), phonon replicas, and multiple electron-side exciton polarons (e.g., A_1^{*-} , A_1^- ; Fig. 4a, c), which are not found in monolayer MoSe₂.

Figure 5e–f displays the splitting energies (ΔE) between A_{1s} and A_1^\pm and between A_{2s} and A_2^\pm at varying gate voltage and Fermi energy (E_F). Their splitting energies at $E_F=0$ (i.e., the exciton-polaron binding energy) and the E_F -dependent slope of ΔE are summarized in Table 2. The ΔE slopes of excited polaron states are considerably larger than those of the ground states, consistent with our observation in monolayer MoSe₂.

We have calculated ΔE on the hole side for monolayer WSe₂ by using the same exciton-polaron theory as in monolayer MoSe₂ but with different material parameters and different best-fit values of the screening reduction parameter (f) (see the details in Supplementary Note 7). The calculated ΔE (lines in Fig. 5f) matches reasonably the experimental ΔE for both the ground and excited states. The results strongly support the exciton-polaron nature of the states.

In our presentation above, we have distinguished the trion and exciton-polaron pictures by considering the different carrier-density dependence of their binding energy. Actually, our theory also predicts markedly different oscillator strength for the trion and exciton polaron. In a simple explanation, let us consider the creation of a trion (with center-of-mass wave vector \mathbf{k}) from a photo-generated electron-hole pair in the presence of a free carrier (with the same \mathbf{k}) in a system with translational symmetry. In this case, the initial free-carrier state has one single \mathbf{k} value. But once this carrier enters into the trion, its wave vector will be dispersed over a wide range of \mathbf{k} values. The overlap between these two configurations is negligible. As a result, our theory predicts essentially zero oscillator strength for the trion. In comparison, let us consider the creation of an exciton polaron in the presence of a finite FS. In this case, the exciton polaron consists of a bare-exciton component and a Suris-tetron component. The bare-exciton component will bestow the polaron with finite oscillator strength. Therefore, the exciton-polaron model is more reasonable than the trion model to explain the strong optical signals observed in our experiment.

In summary, we have observed gate-tunable exciton-polaron Rydberg states associated with the 1s–3s excitons in monolayer MoSe₂ and WSe₂ devices. Our experimental results and theoretical calculations support the exciton-polaron nature of both the ground and excited excitonic states in charged monolayer MoSe₂ and WSe₂. We expect that exciton polarons

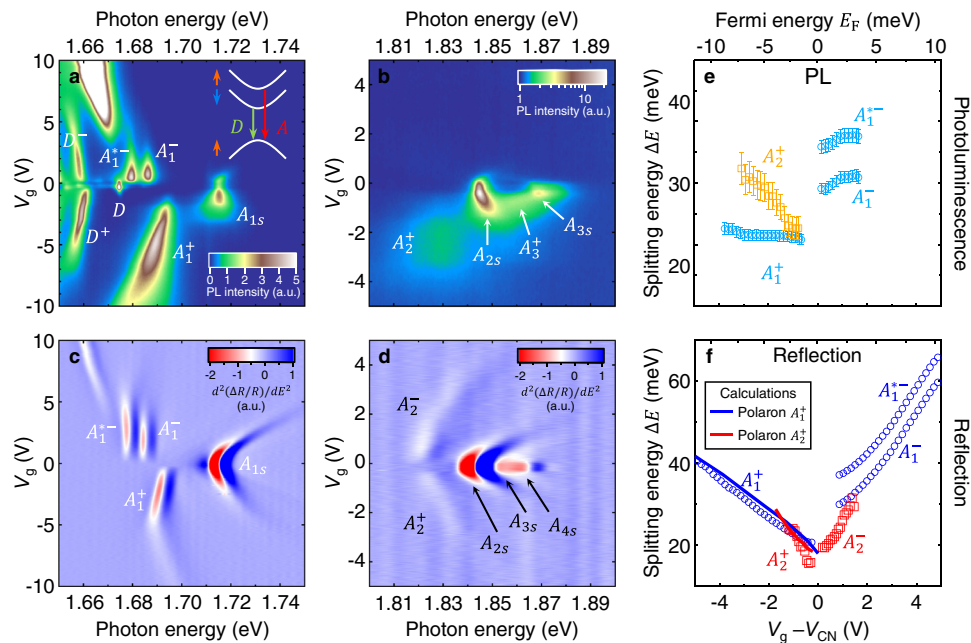


Fig. 5 Optical signatures of exciton-polaron Rydberg states in monolayer WSe₂. **a, b** Gate-dependent PL maps plotted in arbitrary unit (a.u.). The inset in **a** shows the band configurations in monolayer WSe₂. The arrow beside each band denotes its electron spin. The red and green arrows between the bands denote the recombination transitions for bright exciton (A) and dark exciton (D), respectively. **c, d** Gate-dependent maps of the second energy derivative of the reflectance contrast $d^2(\Delta R/R)/dE^2$ plotted in arbitrary unit (a.u.). **e** Gate-dependent PL energy separation between A_1^+ , A_1^- , A_1^{*-} and A_{1s} (cyan circles) and between A_2^+ and A_{2s} (orange squares) in **a, b**. The error bars (not shown if smaller than the symbols) represent the uncertainty in fitting the PL spectra with multiple Lorentzian functions. **f** Gate-dependent energy separation between A_1^+ , A_1^- , A_1^{*-} and A_{1s} (blue circles) and between A_2^+ and A_{2s} (red squares) in the $d^2(\Delta R/R)/dE^2$ maps in **c, d**. We subtract the charge-neutrality gate voltage $V_{CN} \approx -0.14$ V from the applied gate voltage V_g . The blue (red) solid line is the calculated A_1^+ (A_2^+) binding energy by our theoretical model of exciton polarons. The measurements were made at temperature $T \approx 15$ K with no magnetic field.

Table 2 Measured binding energies of exciton polarons for monolayer WSe₂.

		A_1^-	A_1^{*-}	A_1^+	A_2^-	A_2^+
PL	$\Delta E (E_F = 0)$	29.0 ± 0.1	35.8 ± 0.1	20.5 ± 0.1	—	18.4 ± 0.3
	$d(\Delta E)/dE_F$	1.2 ± 0.1	1.2 ± 0.1	-0.18 ± 0.02	—	-1.8 ± 0.1
Reflection	$\Delta E (E_F = 0)$	27.1 ± 0.1	34.7 ± 0.1	17.5 ± 0.1	17.8 ± 0.4	9.2 ± 0.7
	$d(\Delta E)/dE_F$	2.3 ± 0.1	1.9 ± 0.1	-1.74 ± 0.03	4.7 ± 0.3	-5.5 ± 0.4

$\Delta E (E_F = 0)$ denotes the energy separation (in the unit of meV) between the exciton and exciton polaron at the charge neutrality point. $d(\Delta E)/dE_F$ denotes the slope of ΔE with respect to the Fermi energy (E_F).

also exist in some other 2D semiconductors with finite charge density. Our findings shall motivate further exploration of exciton polarons and complex many-body interactions in different 2D semiconductors.

Note added in proof: We were aware of two related papers on the topic of exciton polarons (ref. 43,44).

Methods

Device fabrication. We fabricate monolayer MoSe₂ and WSe₂ devices encapsulated by hexagonal BN by stacking different component 2D materials together. We first exfoliate monolayers MoSe₂ or WSe₂, multilayer graphene, and thin BN flakes from their bulk crystals onto the Si/SiO₂ substrates (The MoSe₂ and WSe₂ crystals were bought from HQ Graphene Inc.). Afterward, we apply the polycarbonate-based dry-transfer technique to stack them together^{45,46}. In this method, we use a stamp to first pick up a BN flake and then use the BN flake to sequentially pick up two pieces of multilayer graphene (as the contact electrodes), a MoSe₂ (or WSe₂) monolayer, a BN thin layer (as the bottom gate dielectric), and a graphene multilayer (as the back-gate electrode). Our method ensures that the MoSe₂ (or WSe₂) layer does not contact the polymers during the whole fabrication process, so as to reduce the contaminants and bubbles on the interfaces⁴⁷. Standard electron beam lithography is then applied to pattern and deposit the gold contacts (100-nm thickness). Finally, we anneal the devices at 300 °C for 3 h in an argon

environment. Supplementary Fig. 1 shows the schematic and optical image of a representative BN-encapsulated monolayer MoSe₂ device.

Determination of carrier density and Fermi energy. We measure the BN thickness in our devices by atomic force microscopy (AFM). For the monolayer MoSe₂ device in Figs. 2–4, the thickness for the bottom BN is ~ 26 nm. The injected charge density (N) is calculated with the formula $N = CV_g$, where $C = \epsilon\epsilon_0/d$ is the capacitance, d is the thickness of the bottom BN, $\epsilon = 3.1$ is the dielectric constant of BN⁴⁸, and ϵ_0 is the permittivity of free space. We convert the gate voltage into the Fermi energy by using the relation $E_F = \hbar^2 \pi n / m_{e,h}$, where m_e (m_h) is the electron (hole) effective mass. We adopt $m_e = 0.88m_0$ and $m_h = 0.74m_0$ (m_0 is the free electron mass) for monolayer MoSe₂ by fitting our diamagnetic shift with our model calculation. These effective masses are roughly consistent with prior studies⁴⁹. In our experiment on monolayer MoSe₂, the Fermi level shifts with the gate voltage with a slope of $dE_F/dV_g \approx 1.80$ meV/V (2.13 meV/V) on the electron (hole) side.

For the monolayer WSe₂ device in Fig. 5, the thickness of the bottom BN is ~ 40 nm. We use the effective masses $m_e = 0.46m_0$ for the lower conduction band, $m_e = 0.38m_0$ for the upper conduction band, and $m_h = 0.42m_0$ for the top valence band⁸. The Fermi level as a function of gate voltage has a slope of $dE_F/dV_g \approx 2.23$ meV/V (2.44 meV/V) on the electron (hole) side.

Experimental methods. The optical experiments with no magnetic field (Figs. 3–5) were performed in our laboratory at the University of California,

Riverside. We mount the devices in a cryostat (Montana Instruments) with sample temperature at $T \approx 15$ K. For the reflectance contrast measurements, we focus the white light from a broadband light source (Thorlabs, SLS201L) onto the sample with a spot diameter of ~ 2 μm . We measure the reflected spectrum (R_s) from the monolayer MoSe_2 (or WSe_2) sample on the BN/ MoSe_2 /BN/Gr/ SiO_2 /Si stack and a reference spectrum (R_r) on a nearby area without MoSe_2 on the BN/ BN /Gr/ SiO_2 /Si stack. The reflectance contrast ($\Delta R/R$) is obtained as $\Delta R/R = (R_s - R_r)/R_r$. We further take the second energy derivative of the $\Delta R/R$ spectrum to sharpen the weak features.

For the PL experiment with no magnetic field, we excite the samples with a 532-nm continuous laser (Torus 532, Laser Quantum). The laser beam is focused through a microscope objective (NA = 0.6) onto the sample with a spot diameter of ~ 1 μm . The PL is collected through the same objective in a backscattering geometry and analyzed by a high-resolution spectrometer (Princeton Instruments, IsoPlane 320) with a charge-coupled-device (CCD) camera.

The PL experiments with magnetic field were performed in the National High Magnetic Field Laboratory (NHMFL) in Florida, USA. We use a 31-Tesla DC magnet and a fiber-based probe (the same set-up as in ref. 29). The sample temperature is $T = 4$ K. A 532-nm continuous laser is directed through a single-mode optical fiber and focused by a lens (NA = 0.67) onto the sample. The sample is mounted on a three-dimensional Attocube piezoelectric translational stage. The PL is collected through a 50/50 beam splitter into a multimode optical fiber and subsequently measured by a spectrometer (Princeton Instruments, IsoPlane 320) with a CCD camera.

Data availability

The data that support the findings of this study are available from the corresponding authors upon reasonable request.

Received: 15 June 2020; Accepted: 28 September 2021;

Published online: 21 October 2021

References

- Lampert, M. A. Mobile and immobile effective-mass-particle complexes in nonmetallic solids. *Phys. Rev. Lett.* **1**, 450–453 (1958).
- Suris, R. A. et al. Excitons and trions modified by interaction with a two-dimensional electron gas. *Phys. Status Solidi (B)* **227**, 343–352 (2001).
- Thilagam, A. Two-dimensional charged-exciton complexes. *Phys. Rev. B* **55**, 7804–7808 (1997).
- Kheng, K. et al. Observation of negatively charged excitons X^- in semiconductor quantum-wells. *Phys. Rev. Lett.* **71**, 1752–1755 (1993).
- Hartmann, A., Ducommun, Y., Kapon, E., Hohenester, U. & Molinari, E. Few-particle effects in semiconductor quantum dots: observation of multicharged excitons. *Phys. Rev. Lett.* **84**, 5648–5651 (2000).
- Otterburg, T. et al. Enhancement of the binding energy of charged excitons in disordered quantum wires. *Phys. Rev. B* **71**, 033301 (2005).
- Matsunaga, R., Matsuda, K. & Kanemitsu, Y. Observation of charged excitons in hole-doped carbon nanotubes using photoluminescence and absorption spectroscopy. *Phys. Rev. Lett.* **106**, 037404 (2011).
- Mak, K. F. et al. Tightly bound trions in monolayer MoS_2 . *Nat. Mater.* **12**, 207 (2013).
- Jones, A. M. et al. Optical generation of excitonic valley coherence in monolayer WSe_2 . *Nat. Nanotechnol.* **8**, 634 (2013).
- Ross, J. S. et al. Electrical control of neutral and charged excitons in a monolayer semiconductor. *Nat. Commun.* **4**, 1474 (2013).
- Lui, C. H. et al. Trion-induced negative photoconductivity in monolayer MoS_2 . *Phys. Rev. Lett.* **113**, 166801 (2014).
- Suris, R. A. Optical Properties of 2D Systems with Interacting Electrons. SE-9. NATO Science Series. Vol. 119, 111–124 (Springer, Netherlands, 2003).
- Koudinov, A. V. et al. Suris tetrons: possible spectroscopic evidence for four-particle optical excitations of a two-dimensional electron gas. *Phys. Rev. Lett.* **112**, 147402 (2014).
- Chang, Y.-C., Shiau, S.-Y. & Combescot, M. Crossover from trion-hole complex to exciton-polaron in n-doped two-dimensional semiconductor quantum wells. *Phys. Rev. B* **98**, 235203 (2018).
- Efimkin, D. K. & MacDonald, A. H. Exciton-polarons in doped semiconductors in a strong magnetic field. *Phys. Rev. B* **97**, 235432 (2018).
- Efimkin, D. K. & MacDonald, A. H. Many-body theory of trion absorption features in two-dimensional semiconductors. *Phys. Rev. B* **95**, 035417 (2017).
- Sidler, M. et al. Fermi polaron-polaritons in charge-tunable atomically thin semiconductors. *Nat. Phys.* **13**, 255 (2017).
- Fey, C., Schmelcher, P., Imamoglu, A. & Schmidt, R. Theory of exciton-electron scattering in atomically thin semiconductors. *Phys. Rev. B* **101**, 195417 (2020).
- Kang, M. et al. Holstein polaron in a valley-degenerate two-dimensional semiconductor. *Nat. Mater.* **17**, 676–680 (2018).
- Cotlet, O., Wild, D. S., Lukin, M. D. & Imamoglu, A. Rotons in optical excitation spectra of monolayer semiconductors. *Phys. Rev. B* **101**, 205409 (2020).
- Wang, G. et al. Exciton states in monolayer MoSe_2 : impact on interband transitions. *2D Mater.* **2**, 045005 (2015).
- Chernikov, A. et al. Exciton binding energy and nonhydrogenic Rydberg series in monolayer WS_2 . *Phys. Rev. Lett.* **113**, 076802 (2014).
- Chernikov, A. et al. Electrical tuning of exciton binding energies in monolayer WS_2 . *Phys. Rev. Lett.* **115**, 126802 (2015).
- Gupta, G., Kallatt, S. & Majumdar, K. Direct observation of giant binding energy modulation of exciton complexes in monolayer MoSe_2 . *Phys. Rev. B* **96**, 081403 (2017).
- Raja, A. et al. Coulomb engineering of the bandgap and excitons in two-dimensional materials. *Nat. Commun.* **8**, 15251 (2017).
- Han, B. et al. Exciton states in monolayer MoSe_2 and MoTe_2 probed by upconversion spectroscopy. *Phys. Rev. X* **8**, 031073 (2018).
- Goryca, M. et al. Revealing exciton masses and dielectric properties of monolayer semiconductors with high magnetic fields. *Nat. Commun.* **10**, 4172 (2019).
- Molas, M. R. et al. Energy spectrum of two-dimensional excitons in a nonuniform dielectric medium. *Phys. Rev. Lett.* **123**, 136801 (2019).
- Liu, E. et al. Magnetophotoluminescence of exciton Rydberg states in monolayer WSe_2 . *Phys. Rev. B* **99**, 205420 (2019).
- Stier, A. V. et al. Magneto-optics of exciton Rydberg states in a monolayer semiconductor. *Phys. Rev. Lett.* **120**, 057405 (2018).
- Arora, A. et al. Excited-state trions in monolayer WS_2 . *Phys. Rev. Lett.* **123**, 167401 (2019).
- Chen, S.-Y. et al. Luminescent emission of excited Rydberg excitons from monolayer WSe_2 . *Nano Lett.* **19**, 2464–2471 (2019).
- Chen, S.-Y. et al. Superior valley polarization and coherence of 2s excitons in monolayer WSe_2 . *Phys. Rev. Lett.* **120**, 046402 (2018).
- Jones, A. M. et al. Excitonic luminescence upconversion in a two-dimensional semiconductor. *Nat. Phys.* **12**, 323 (2015).
- Liu, E. et al. Gate tunable dark trions in monolayer WSe_2 . *Phys. Rev. Lett.* **123**, 027401 (2019).
- Li, Z. et al. Direct observation of gate-tunable dark trions in monolayer WSe_2 . *Nano Lett.* **19**, 6886–6893 (2019).
- He, M. et al. Valley phonons and exciton complexes in a monolayer semiconductor. *Nat. Commun.* **11**, 618 (2020).
- Liu, E. et al. Valley-selective chiral phonon replicas of dark excitons and trions in monolayer WSe_2 . *Phys. Rev. Res.* **1**, 032007 (2019).
- Liu, E. et al. Multipath optical recombination of intervalley dark excitons and trions in monolayer WSe_2 . *Phys. Rev. Lett.* **124**, 196802 (2020).
- Zhang, X.-X. et al. Magnetic brightening and control of dark excitons in monolayer WSe_2 . *Nat. Nanotech.* **12**, 883 (2017).
- Zhang, X.-X., You, Y., Zhao, S. Y. F. & Heinz, T. F. Experimental evidence for dark excitons in monolayer WSe_2 . *Phys. Rev. Lett.* **115**, 257403 (2015).
- Wang, G. et al. In-plane propagation of light in transition metal dichalcogenide monolayers: optical selection rules. *Phys. Rev. Lett.* **119**, 047401 (2017).
- Goldstein, T. et al. Ground and excited state exciton polarons in monolayer MoSe_2 . *J. Chem. Phys.* **153**, 071101 (2020).
- Wagner, K. et al. Autoionization and Dressing of Excited Excitons by Free Carriers in Monolayer WSe_2 . *Phys. Rev. Lett.* **125**, 267401 (2020).
- Hunt, B. et al. Massive Dirac fermions and Hofstadter butterfly in a van der Waals heterostructure. *Science* **340**, 1427–1430 (2013).
- Wang, L. et al. One-dimensional electrical contact to a two-dimensional material. *Science* **342**, 614–617 (2013).
- Purdie, D. G. et al. Cleaning interfaces in layered materials heterostructures. *Nat. Commun.* **9**, 5387 (2018).
- Liu, E. et al. Landau-quantized excitonic absorption and luminescence in a monolayer valley semiconductor. *Phys. Rev. Lett.* **124**, 097401 (2020).
- Larentis, S. et al. Large effective mass and interaction-enhanced Zeeman splitting of K-valley electrons in MoSe_2 . *Phys. Rev. B* **97**, 201407(R) (2018).

Acknowledgements

We thank Hongyi Yu, Wang Yao, Allen P. Mills, Dmitry K. Efimkin, and Allan H. MacDonald for discussions; Nathaniel M. Gabor and Yong-Tao Cui for co-supporting E.L.; and Harry W. K. Tom for equipment support. C.H.L. acknowledges support from the National Science Foundation Division of Materials Research CAREER Award No. 1945660 and the American Chemical Society Petroleum Research Fund (ACS PRF No. 61640-ND6). Y.-C.C. acknowledges support from the Ministry of Science and Technology (Taiwan) under grant Nos. MOST 108-2112-M-001-041 and 109-2112-M-001-046. K.W. and T.T. acknowledge support from the Elemental Strategy Initiative conducted by the MEXT, Japan and the CREST (JPMJCR15F3), JST. A portion of this work was performed at the National High Magnetic Field Laboratory, which is supported by the National Science Foundation Cooperative Agreement No. DMR-1644779 and the State of Florida.

Author contributions

E.L. fabricated the devices. J.v.B. established experimental facilities for the research. E.L. and J.v.B. performed the experiments and analyzed the data. Z.L. and D.S. supported the magneto-optical experiment. T.T. and K.W. provided boron nitride crystals for device fabrication. Y.-C.C. did the theoretical calculations. C.H.L. supervised the project. C.H.L., E.L., and Y.-C.C. wrote the manuscript.

Competing interests

The authors declare no competing interests.

Additional information

Supplementary information The online version contains supplementary material available at <https://doi.org/10.1038/s41467-021-26304-w>.

Correspondence and requests for materials should be addressed to Yia-Chung Chang or Chun Hung Lui.

Peer review information *Nature Communications* thanks the anonymous reviewers for their contribution to the peer review of this work.

Reprints and permission information is available at <http://www.nature.com/reprints>

Publisher's note Springer Nature remains neutral with regard to jurisdictional claims in published maps and institutional affiliations.



Open Access This article is licensed under a Creative Commons Attribution 4.0 International License, which permits use, sharing, adaptation, distribution and reproduction in any medium or format, as long as you give appropriate credit to the original author(s) and the source, provide a link to the Creative Commons license, and indicate if changes were made. The images or other third party material in this article are included in the article's Creative Commons license, unless indicated otherwise in a credit line to the material. If material is not included in the article's Creative Commons license and your intended use is not permitted by statutory regulation or exceeds the permitted use, you will need to obtain permission directly from the copyright holder. To view a copy of this license, visit <http://creativecommons.org/licenses/by/4.0/>.

© The Author(s) 2021